J. Fluid Mech. (1991), *vol.* 230, *pp.* 245–269
Printed in Great Britain

Instability and transition of disturbed flow over a rotating disk

By ALAN J. FALLER

Institute for Physical Science and Technology, University of Maryland, College Park, MD 20742, USA

(Received 20 July 1990 and in revised form 15 February 1991)

Disturbed flow over a rotating disk can lead to transition of the von Kármán boundary layer at a much lower Reynolds number, *Re*, (i.e. smaller radius) than that due to the well-known Type 1 stationary mode of instability. This early transition is due to the excitation of the Type 2 instability, similar to that found in the Ekman layer. Detailed numerical values of the growth rates, phase speeds, group velocities, neutral curves, and other characteristics of these two instabilities have been calculated over a wide range of parameters. Neutral curves for the Ekman and Bödewadt boundary layers also are presented. The minimum critical Reynolds numbers for the von Kármán, Ekman and Bödewadt layers are $Re_{c(2)} = 69.4$, 54.3, and 15.1 with wavelengths $L = 22.5$, 20.1, and 16.6 and at angles $\epsilon = -19.0°$, $-23.1°$, and $-33.2°$, respectively. These minimum critical values frequently do not well describe laboratory observations, however, because at larger *Re* other modes grow more rapidly and dominate the flow.

The computed results are in excellent agreement with laboratory observations wherever comparison is possible. The growth of representative Type 1 instabilities with radius is shown to lead to *N*-factors greater than 9 at $Re = 520$ as appears to be necessary for transition to turbulence by the interaction of Type 1 with the basic flow. The growth of Type 2 instabilities with radius can lead to three additional mechanisms of transition. The necessary levels of excitation of Type 2 for these different mechanisms are estimated.

A sequence of photographs from a ciné film illustrate one of the transition mechanisms discussed: the interaction of Type 2 instabilities and a secondary instability that is nearly perpendicular to the Type 2 vortices.

1. Introduction

The von Kármán layer, the boundary layer flow due to a rotating disk in an otherwise stationary fluid, has long been a prototype for studies of instability and transition in general three-dimensional boundary layers. The instability that appears in the form of stationary spiral vortices was first studied by Smith (1947). Gregory, Stuart & Walker (1955) discussed the application to swept-back airfoils, performed well-controlled experiments to find critical values of the Reynolds numbers for instability (Re_c) and for transition (Re_t), and developed a partial theory showing that those vortices were associated with an inflexion point in the cross-vortex basic flow. This instability was referred to as Type 1 by Faller & Kaylor (1966*a*) who found that the von Kármán layer has a second instability that is analogous to the Type 2 instability of the Ekman layer (Faller 1963; Faller & Kaylor 1966*a*, *b*). Type 2 as well as Type 1 has the form of spiral vortices but of the opposite angle relative to circles on the disk and with a lower value of Re_c, and the vortices move rapidly outward, amplifying as they progress. Lilly (1966) independently found this instability in his numerical solutions of the eigenvalue problem for the Ekman layer. He referred to it as the 'parallel mode' of instability and showed that the mechanism involves Coriolis forces rather than the inflexion point. Type 2 also has been found in diverse situations, as for example in the flow in a spherical gap (Büeler & Zierep 1983).

Type 2 was not found by Gregory *et al.* (1955) for two reasons. First, their observational techniques were suited primarily for detection of the known stationary vortices. Second, because any disturbance of air in the room raised havoc with their determination of a consistent value of Re_t, they were extraordinarily careful to assure disturbance-free conditions. In Faller & Kaylor (1966*a*) it was found that external disturbances easily excite Type 2 instabilities, and it is likely that in the Gregory *et al.* (1955) experiments early transition arose from the excitation of this unknown instability. A major goal of this paper is to assess the mechanism(s) by which external disturbances lead to early transition and the role(s) played by the Type 2 instability.

In the Ekman-layer experiments of Faller (1963) (in water) Type 2 instabilities appeared consistently only when there were mechanical disturbances of the experiment. This dependency was verified in rotating disk studies (also in water, Faller & Kaylor 1966*a*) where only Type 1 appeared if the experiments were performed carefully and where Type 2 appeared more or less in proportion to the strength of disturbances.

As with the Tollmien–Schlichting waves a Type 2 vortex (or wave) in the von Kármán layer amplifies as it moves toward larger Re. Thus it requires triggering to attain an observable amplitude close to its critical value, $Re_{c(2)}$. But the Type 2 vortices of three-dimensional boundary layers should not be confused with or referred to as a Tollmien–Schlichting instability. Type 2 has a different dynamical mechanism that is dependent upon centrifugal and/or Coriolis forces, and the vortices are nearly parallel, not perpendicular, to the free-stream flow. Also note that the growth rate of Type 2 as $Re \rightarrow \infty$ depends upon the method of scaling time (Appendix A).

The disturbed flow due to instabilities may sometimes be referred to as waves and sometimes as vortices. The disturbances have vorticity, and when the basic flow is subtracted from the total flow they appear as vortices. But in terms of the total flow, the instability appears as a waviness of the streamlines; and in visualization experiments dye in the lower part of the boundary layer takes on a wavy character. Moreover, the propagation of energy appears to follow the usual kinematic formulae, originally derived for waves, by which the group velocity is related to the phase speed. Therefore a description as waves often seems to be appropriate.

The experiments in water (Faller & Kaylor 1966*a*) showed a specific mechanism for transition to turbulence that involved Type 2 vortices and a secondary instability. When the primary vortices attained a sufficient amplitude, a high-wavenumber secondary instability, then referred to as 'gills', formed nearly perpendicular to the primary vortices. (The term 'ribs', as later suggested by other authors, seems more appropriate and will be used hereafter). Once formed, the two sets of vortices interacted rapidly to produce turbulence. This occurred well below $Re_{c(1)}$ as known at that time. Detailed data on the primary (Type 2) and secondary vortices are discussed in §7.

Many studies have been concerned with Type 1 and it has been found that the china clay technique of Gregory *et al.* (1955) and other visual methods greatly overestimated $Re_{c(1)}$. Most recently Malik, Wilkinson & Orszag (1981), Wilkinson & Malik (1985), Mack (1985), and Malik (1986) have shown that experimental and numerical studies are in approximate agreement and have converged on the value $Re_{c(1)} = 285$. In Malik *et al.* (1981) it was briefly mentioned that there appeared to be a critical value for a non-stationary instability at $Re = 50$, but further information on that instability was not provided and its possible significance for transition was not considered.

In this paper I present a summary of new numerical calculations of the instabilities over a rotating disk, emphasizing Type 2, and a description of four plausible mechanisms of transition to turbulence. The mechanism selected in any particular experiment should depend upon the level of excitation of Type 2 by disturbances in the external flow. More extensive results, upon which this paper is based, are contained in recent technical notes (Faller, Yang & Piomelli 1989; Faller 1990).

2. The theoretical model

Consider the flow induced in a homogeneous fluid rotating at angular speed ω_f by a disk rotating at angular speed ω_b about the same axis of rotation. The radius of the disk and the extent of the fluid above the disk are taken to be infinite. The von Kármán layer arises for $\omega_f = 0$, $\omega_b \neq 0$, the Bödewadt layer occurs when $\omega_b = 0$, $\omega_f \neq 0$, and the Ekman layer is found when $\omega_b \approx \omega_f$. To incorporate this range of conditions in one model, a 'system rotation rate', Ω, is defined by

$$\Omega = \omega_f/(2-\Delta\omega/\Omega)+\omega_b/(2+\Delta\omega/\Omega), \tag{1}$$

where $\Delta\omega = \omega_f - \omega_b$, or solving explicitly for Ω,

$$\Omega = \Sigma\omega/4+((\Sigma\omega/4)^2+(\Delta\omega)^2/2)^{\frac{1}{2}} \tag{2}$$

where $\Sigma\omega = \omega_f + \omega_b$.

A characteristic boundary-layer depth applicable to all cases is given by $D = (\nu/\Omega)^{\frac{1}{2}}$ where ν is the kinematic viscosity. An appropriate Rossby number is $Ro = \Delta\omega/\Omega$, and a useful non-dimensional Coriolis parameter is $Co = 2 - Ro - Ro^2$.

The following steps summarize the manipulation of the Navier–Stokes equations and the method of solution:

(i) The equations in polar coordinates are separated into those of a basic flow and fluctuation equations. The basic flow is the axially symmetrical similarity solution taken relative to the rotating boundary. The equations are made non-dimensional.

(ii) The basic flow equations are solved numerically, and the fluctuation equations are linearized to form perturbation equations.

(iii) The radial and tangential components of the perturbation vorticity equation are derived.

(iv) The perturbation equations are converted to a local rectangular (x, y) coordinate system centred at some fixed value of r with x along the radial direction.

(v) The 'rectangularized' equations are rotated about the z-axis so that the new x-axis is at an angle ϵ with respect to the tangential direction. Instabilities are assumed to be two-dimensional vortices independent of the rotated x-axis.

(vi) The equations to be solved now comprise the time-dependent perturbation equations for the x-component of velocity, u, and the x-component of vorticity, ξ, plus the Poisson equation relating ξ to a stream function, ϕ, in the (y, z)-plane.

(vii) The boundary conditions are no slip at $z = 0$, free slip at $z = H \gg D$, and periodicity in y. Dependent variates are represented as harmonic waves of wavelength L in y, and the independent variates are thus reduced to z and t (time).

(viii) The equations are integrated in t on a vertical grid for selected values of the parameters Re, ϵ, and L (starting with randomized initial values) until a constant rate of growth, α, of the perturbation kinetic energy and a constant phase speed of the disturbance, C_{p}, are attained.

The component equations of motion for a uniform fluid in a cylindrical polar coordinate system rotating with the angular speed ω_{b} may be written as

$$\tilde{u}_t + (\tilde{\mathbf{u}}\cdot\nabla)\,\tilde{u} - \frac{\tilde{v}^2}{r} - 2\omega_{\mathrm{b}}\,\tilde{v} = -\tilde{p}_r + \nu\left(\nabla^2\tilde{u} - \frac{\tilde{u}}{r^2} - \frac{2\tilde{v}_\theta}{r^2}\right), \tag{3}$$

$$\tilde{v}_t + (\tilde{\mathbf{u}}\cdot\nabla)\,\tilde{v} + \frac{\tilde{u}\tilde{v}}{r} + 2\omega_{\mathrm{b}}\,\tilde{u} = -\frac{\tilde{p}_\theta}{r} + \nu\left(\nabla^2\tilde{v} - \frac{\tilde{v}}{r^2} + \frac{2\tilde{u}_\theta}{r^2}\right), \tag{4}$$

$$\tilde{w}_t + (\tilde{\mathbf{u}}\cdot\nabla)\,\tilde{w} = -\tilde{p}_z + \nu\nabla^2\tilde{w}, \tag{5}$$

and the continuity equation is

$$(r\tilde{u})_r/r + \tilde{v}_\theta/r + \tilde{w}_z = 0, \tag{6}$$

where $\tilde{u}$, $\tilde{v}$, and $\tilde{w}$ are the components of the velocity $\tilde{\mathbf{u}}$ in the r, θ, and z directions, respectively, the constant specific gravity is included with the pressure as p; and the subscripts t, r, θ, and z denote partial differentiation. The fluid in the semi-infinite domain $z > 0$ is rotating at angular speed ω_{f} except for the boundary-layer effects of the differential rotation, $\Delta\omega$.

The dependent variates are separated into those of a basic flow (capitals) and fluctuations, as

$$(\tilde{u}, \tilde{v}, \tilde{w}, \tilde{p}) = (U, V, W, P) + (u, v, w, p). \tag{7}$$

The basic-flow equations that corresponds to (3)–(6) are found by substituting (7) and by setting $(u, v, w, p) = 0$. Assuming an axially symmetrical similarity solution to the basic flow with the similarity variates $F(z,t)$, $G(z,t)$ and $H(z,t)$ defined by

$$U = \Delta\omega rF, \quad V = \Delta\omega rG, \quad W = \Delta\omega DH \tag{8}$$

and scaling lengths by D and time by Ω^{-1}, the radial basic flow equation is

$$F_t + Ro(F^2 - G^2 + HF_z) - CoG = -P^*_r + F_{zz}, \tag{9}$$

where t and z are now dimensionless, and $P^* = \Delta\omega\Omega rDP$ is a suitably defined non-dimensional pressure whose radial gradient can be determined from the relative tangential flow as $z \to \infty$. There $V = \Delta\omega r$ and $F = F_z = F_{zz} = 0$, so $P^* = Ro + Co$. Then the basic flow equations that arise from (3) and (4) are

$$F_t + Ro(F^2 + HF_z - (G^2 - 1)) - Co(G - 1) - F_{zz} = 0, \tag{10}$$

$$G_t + Ro(2FG + HG_z) + CoF - G_{zz} = 0, \tag{11}$$

and from (6) one obtains

$$H = -2\int_0^z F(z')\,\mathrm{d}z'. \tag{12}$$

Equations (10)–(12) were solved as time-dependent equations on a uniform grid typically with $\Delta z = 0.1$ and with 400 points, until steady-state values of F, G, and H were attained.

The non-dimensional perturbation equations are found by: (i) subtracting the basic flow equations from (3)–(6), (ii) omitting products of fluctuations, and (iii) introducing the transformations

$$(u,v,w)\rightarrow \Delta\omega D(u,v,w),\quad (r,z)\rightarrow D(r,z),\quad t\rightarrow t/\Omega,\quad p\rightarrow \Delta\omega\Omega D^2 p, \tag{13}$$

where the right-hand-side variates are dimensionless. The non-dimensional perturbation equations are then

$$u_t+Re\left(Fu_r+\frac{Gu_\theta}{r}+wF_z\right)+Ro(Hu_z+Fu+2Gw)-Co\,v=-p_r+\nabla^2u-\frac{u}{r^2}-\frac{2v_\theta}{r^2}, \tag{14}$$

$$v_t+Re\left(Fv_r+\frac{Gv_\theta}{r}+wG_z\right)+Ro(Hv_z+Fv+2Gu)+Co\,u=-\frac{p_\theta}{r}+\nabla^2v-\frac{v}{r^2}+\frac{2u_\theta}{r^2}, \tag{15}$$

$$w_t+Re(Fw_r+Gw_\theta/r)+Ro(Hw_z+wH_z)=-p_z+\nabla^2w, \tag{16}$$

$$(ru)_r/r+v_\theta/r+w_z=0, \tag{17}$$

where Re is defined and related to Ro by

$$Re=(\Delta\omega r_{\mathrm{d}})D/\nu=\Delta\omega r/\Omega=r\,Ro \tag{18}$$

and where r_{d} is the dimensional radius. All variates are dimensionless from (18) onward.

Note that for the von Kármán layer, since $\Delta\omega=-\omega_{\mathrm{b}}$, $\Omega=\omega_{\mathrm{b}}$, $Ro=-1$, so $Re=-r$ and is negative. But for convenience Re will be generally treated as a positive number except where the negative is necessary.

The method of solution requires the adoption of a local rectangular coordinate system (centred at some fixed value of Re) and to this end let $\mathrm{d}r\rightarrow\mathrm{d}x$ and $r\,\mathrm{d}\theta\rightarrow\mathrm{d}y$. Consistent with this rectangularization some terms that would arise from use of the polar form of continuity have been dropped, and the $1/r$ and $1/r^2$ viscous terms have been omitted because $1/r=-1/Re$. The rectangularized horizontal-component vorticity equations, derived from (14)–(16), are then

$$\xi_t+Re(F\xi_x+G\xi_y-wG_{zz}-F_zv_x+G_zw_x)+Ro(H\xi-Fv-2Gu)_z-Co\,u_z=\nabla^2\xi, \tag{19}$$

$$\eta_t+Re(F\eta_x+G\eta_y+wF_{zz}-F_zv_y+G_zw_y)+Ro(H\eta+Fw-2Gv)_z-Co\,v_z=\nabla^2\eta, \tag{20}$$

where ξ and η are the x (radial) and y (tangential) components of vorticity.

The two pairs of equations, (14) (15) and (19) (20), are now rotated through an angle $\beta=\epsilon+\frac{1}{2}\pi$ as illustrated in figure 1, where ϵ is the angle of the new x-axis with respect to the tangential direction. The instabilities are assumed to be two-dimensional vortices independent of this new x-direction, so in the rotated equations $\partial/\partial x=0$ and only the equations for the new u and ξ need to be retained. The reoriented equations to be solved are

$$u_t+Re(-(FC+GS)\,u_y+(-F_zS+G_zC)\,w)$$
$$+Ro(Hu_z+Fu-2Gv)-Co\,v=u_{yy}+u_{zz}, \tag{21}$$

$$\xi_t+Re(-(FC+GS)\,\xi_y+(F_{zz}C+G_{zz}S)\,w)+Ro(H\xi-Fv-2Gu)_z$$
$$+Ro(FC+GS)\,Cw_y-Co\,u_z=\xi_{yy}+\xi_{zz}, \tag{22}$$

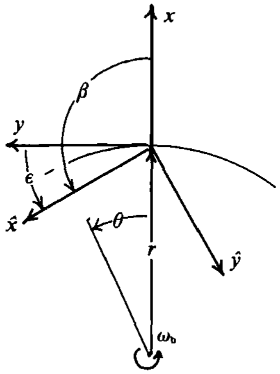

Figure 1. The conversion from polar (r, θ) to rotated rectangular (x, y) coordinates by rotation through the angle $\beta = \epsilon + \frac{1}{2}\pi$. Instabilities are assumed to be two-dimensional vortices independent of $\hat{x}$.

where $C = \cos\epsilon$, $S = \sin\epsilon$. The stream function for the flow in the new (y, z)-plane is defined by

$$w = \phi_y, \quad v = -\phi_z, \quad \xi = \nabla^2\phi. \tag{23}$$

3. Numerical methods

Equations (21)–(23) were solved as in Faller & Kaylor (1966*b*), and the method is only summarized briefly here. The dependent variates u, ξ, and ϕ were taken to be periodic in y with wavelength L and were written as the sum of sine and cosine components. These were represented on a uniformly spaced but staggered vertical grid with ξ and ϕ at the even numbered levels and u, v, and w at the odd levels. The lower boundary was $J = 1$ with $u = v = w = 0$. At the upper boundary, typically $J = 200$ or 400, the conditions were $u_z = 0$, $v_z = 0$, and $w = 0$.

Given specific values for Re, ϵ, and L, the equations for the sine and cosine amplitudes of $\xi(J, t)$ and $u(J, t)$ were integrated over t, using the Adams-Bashforth time-step, centred differences in z, and randomized initial values. Each integration was continued until the solution steadied to a constant $\alpha = \partial K/\partial t$ where K is the total perturbation kinetic energy.

The exaggeration of α by the Adams-Bashforth method due to finite Δt (Faller & Kaylor 1966*b*) was eliminated by reducing Δt in steps to $\frac{1}{2}$, $\frac{1}{4}$, and $\frac{1}{8}$ of its initial value and by then quadratically extrapolating the sequence of values of α to $\Delta t = 0$ (Richardson extrapolation).

Data obtained at selected times included α, C_p, the kinetic energy of the overturning cells,

$$CK = (2HL)^{-1} \int_0^L \int_0^H (v^2 + w^2)\, dy\, dz,$$

the kinetic energy of the x-component of the flow,

$$UK = (2HL)^{-1} \int_0^L \int_0^H u^2\, dy\, dz,$$

where $K = CK + UK$, and the ratio $RK = UK/CK$. This ratio has values of typically about $RK = 20$, thus indicating values of u many times larger than those of v and w. See tables 1 and 2.

		Wavelength, L									
Re		15	20	25	30	35	40	45	50	55	60
480	α	4.479	4.583	3.433	1.972	0.566	0.487	0.804	0.875	0.830	0.736
	C_p	−0.0313	−0.0246	−0.0158	−0.0054	0.0082	0.0253	0.0356	0.0434	0.0498	0.0554
	RK	19.8	15.9	14.1	13.4	13.8	12.7	10.5	8.9	7.7	6.8
400	α	2.613	2.614	1.502	0.046	0	0.100	0.393	0.428	0.374	0.291
	C_p	−0.0325	−0.0255	−0.0159	−0.0036	0	0.0325	0.0405	0.0476	0.0535	0.0590
	RK	19.5	15.9	14.4	14.4	0	11.9	9.3	7.9	6.8	6.0
320	α		0.893								
	C_p		−0.0264								
	RK		16.1								

TABLE 1. The growth rate, α, phase speed, C_p, and ratio, RK, at $\epsilon = 15°$ as a function of Re and L. These results are typical of the Type 1 instability. Values at intervals of 40 in Re, at angles from 20° to −30° in intervals of 5°, and for L from 10 to 60 in intervals of 5 are available in Faller *et al.* (1989).

		Wavelength, L									
Re		15	20	25	30	35	40	45	50	55	60
480	α	–	0.562	1.159	1.434	1.566	1.625	*1.644*	1.637	1.613	1.577
	C_p	–	0.3188	0.3205	0.3226	0.3247	0.3269	0.3291	0.3313	0.3335	0.3356
	RK	–	69.8	48.4	37.7	31.7	27.6	24.6	22.5	20.7	19.2
400	α	–	0.643	1.130	1.360	1.469	1.510	*1.512*	1.488	1.449	1.401
	C_p	–	0.3193	0.3212	0.3236	0.3261	0.3287	0.3312	0.3338	0.3365	0.3390
	RK	–	59.5	42.7	34.1	28.8	25.3	22.6	20.5	18.8	17.4
320	α	–	0.700	1.092	1.272	1.341	*1.349*	1.323	1.276	1.218	1.154
	C_p	–	0.3199	0.3224	0.3253	0.3284	0.3316	0.3349	0.3380	0.3410	0.3439
	RK	–	49.9	37.1	28.5	25.6	22.4	20.0	18.1	16.5	15.2
240	α	0.064	0.735	1.015	1.114	*1.122*	1.084	1.026	0.956	0.882	0.808
	C_p	0.3187	0.3213	0.3248	0.3289	0.3329	0.3369	0.3408	0.3445	0.3482	0.3516
	RK	60.9	40.8	31.2	25.5	21.6	18.8	16.6	14.9	13.5	12.4
160	α	0.226	0.647	*0.764*	0.761	0.709	0.636	0.556	0.475	0.397	0.322
	C_p	0.3204	0.3252	0.3308	0.3363	0.3417	0.3468	0.3516	0.3561	0.3603	0.3643
	RK	44.2	30.8	23.6	19.1	16.0	13.8	12.1	10.8	10.0	9.0
80	α	−0.035	*0.098*	0.086	0.030	−0.042	−0.113	−0.182	−0.246	−0.304	−0.358
	C_p	0.3293	0.3381	0.3464	0.3542	0.3613	0.3676	0.3737	0.3790	0.3839	0.3885
	RK	24.3	17.0	12.9	10.4	8.8	7.5	6.6	5.9	5.4	4.9

TABLE 2. The same as table 1 but for Type 2 at $\epsilon = -15$. Italicized values show the shift of the maximum in α as Re is changed.

As with Δt, Richardson's method was used with $\Delta z = 0.4$ and $\Delta z = 0.2$ to extrapolate results to $\Delta z = 0$. The extrapolated values were often checked with higher resolution calculations, and the final values of α are accurate to better than three decimal places. For the Ekman layer the value of $Re_{c(2)}$ is almost exactly the same as that of Iooss, Nielsen & True (1978), and for the rotating disk $Re_{c(1)}$ is the same as that of Malik (1986). All computations used a Macintosh II.

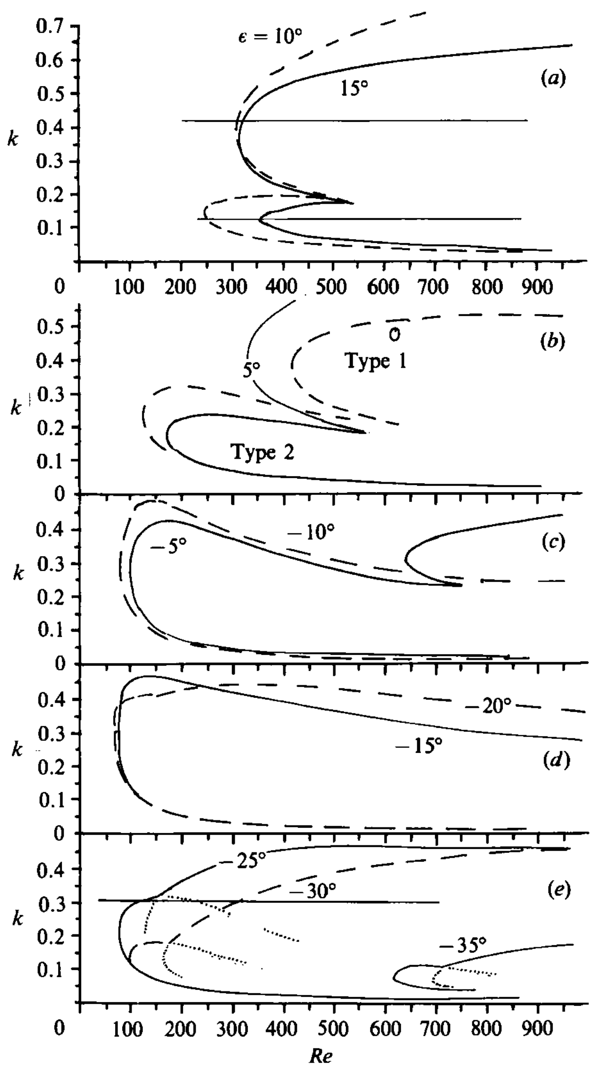

FIGURE 2. Neutral curves ($\alpha = 0$) as a function of Re and k for values of ϵ from 15° to −35°. The Type 1 and Type 2 instabilities are clearly separated in (*a*), (*b*) and (*c*), while (*d*) and (*e*) suggest the superposition of two instability mechanisms, as indicated by the dashed continuation lines. Horizontal lines correspond to the curves of figure 3.

4. Computational results

4.1. *Neutral curves and growth rates*

Figure 2 shows neutral curves as functions of Re and k for several values of ϵ. (Results are discussed in terms of both L and $k = 2\pi/L$, and table 3 gives the conversion.) These were obtained by a curve-following routine that varied Re and k to keep α close to zero. These lengthy computations used $\Delta z = 0.4$ and therefore are slightly in error, but over much of the diagram the errors are comparable to the drafting uncertainties.

The Type 1 and Type 2 instabilities are clearly separated in figures 2(*a*), 2(*b*) and 2(*c*). At $\epsilon = 15$ Type 1 has the lower value of Re_c but at 10° Type 2 has a lower minimum. As ϵ becomes negative Type 1 retreats while Type 2 continues to advance to reach a minimum of $Re_{c(2)} = 69$ at $\epsilon = -19°$. But note that below $\epsilon = -15°$ the

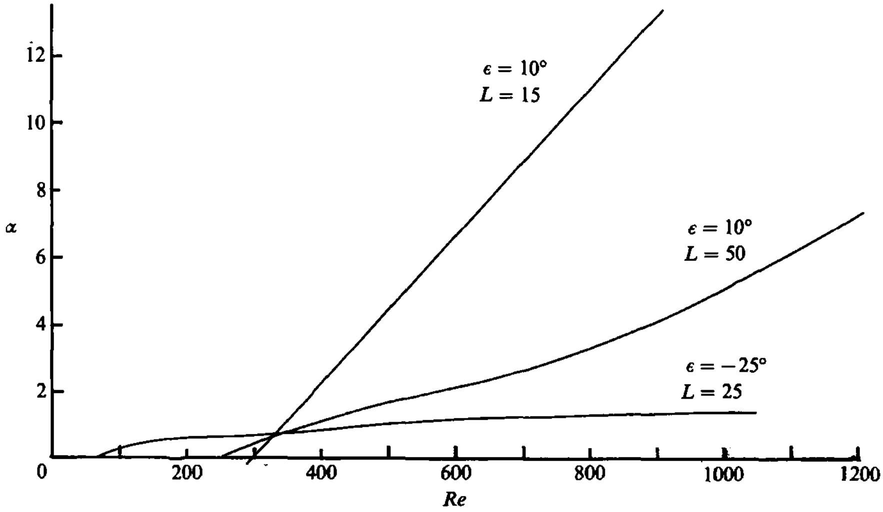

FIGURE 3. The rate of growth of kinetic energy α as a function of *Re* for selected values of ϵ and L.

L	k	k	L
10	0.628	0.10	62.8
15	0.419	0.15	41.9
20	0.314	0.20	31.4
25	0.251	0.25	25.1
30	0.209	0.30	20.9
35	0.180	0.35	18.0
40	0.157	0.40	15.7
45	0.140	0.45	14.0
50	0.126	0.50	12.6
55	0.114	0.55	11.4
60	0.105	0.60	10.5

TABLE 3. Conversions between wavelength L and wavenumber k.

upper branch of the neutral curve rises until $\epsilon = -25°$, and there appear to be first-order discontinuities in the curves at $-25°$, $-30°$ and $-35°$. These patterns suggest that below approximately $\epsilon = -15$ the unstable region may be the superposition of two instabilities. But attempts to clearly distinguish a third instability (discussed in Faller 1990) have been unsuccessful.

Figure 3 shows curves of $\alpha(Re)$ for the three combinations of ϵ and L that are denoted by horizontal lines in figures 2(*a*) and 2(*e*). At $\epsilon = 10°$ and $L = 15$ ($k = 0.419$) we see a linear increase of α with *Re* that is typical of the Type 1 instability (Appendix A). At the same angle but for $L = 50$ the curve of α starts from 0 parabolically as a typical Type 2 instability, but at large *Re* there is a change to the more rapid linear growth typical of Type 1. This may be understood from figure 2(*a*) by noting that an extension of the upper portion of the dashed neutral curve (Type 1, $\epsilon = 10$) probably would dip below the horizontal line at about $Re = 900$.

Figure 4 illustrates $Re_c(\epsilon, k)$ and shows the minimum values $Re_{c(1)} = 285$ and $Re_{c(2)} = 69$. The shaded region, $Re_c > 400$, is a clear demarcation between the two instabilities. Figure 5 gives the patterns of α and C_p at $Re = 400$. Here the maxima

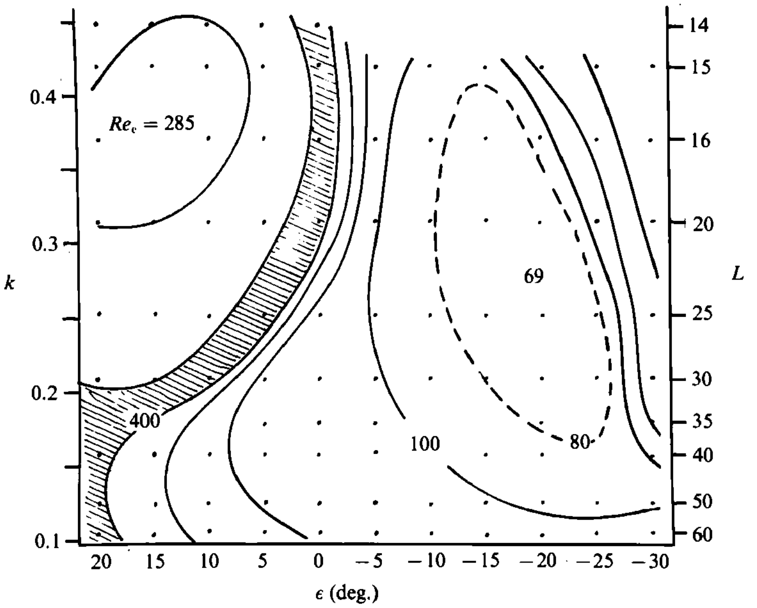

FIGURE 4. Re_c as a function of ϵ and k or L. Minima are $Re_{c(2)} = 69$ found at $k = 0.279$ ($L = 22.5$) and $\epsilon = -19°$, and $Re_{c(1)} = 285.3$ found at $k = 0.378$ ($L = 16.62$) and $\epsilon = 13.9°$. Dots indicate data points for the analysis.

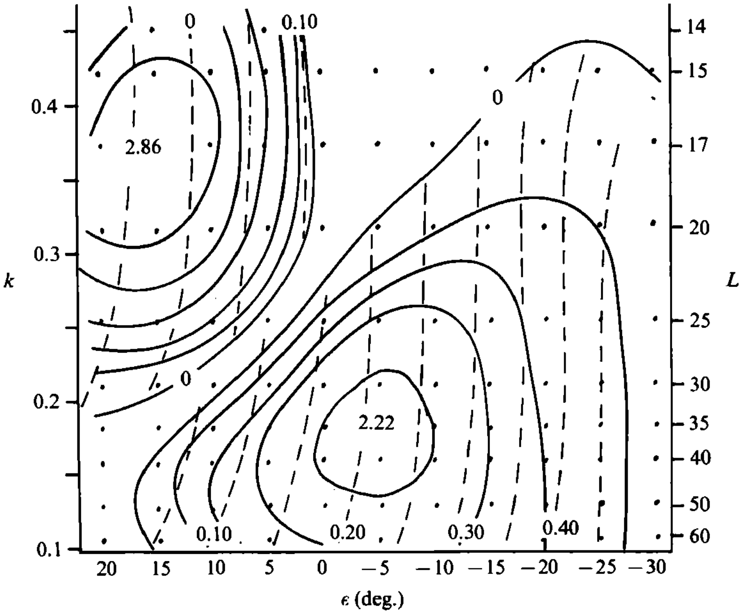

FIGURE 5. The growth rate of kinetic energy, α, at $Re = 400$ (0 lines and maxima labelled) with the coordinates of figure 4. Dashed lines indicate phase speeds, C_p (labelled 0 to 0.40).

of α for Types 1 and 2 are nearly equal despite the large difference in their values of Re_c because of the more rapid linear growth of Type 1. Note the shift of the centre of the contours for Type 2 from figure 4 to figure 5. At $Re = 400$ the maximum for Type 2 has a larger L and larger ϵ. This shift has a bearing on which mode of

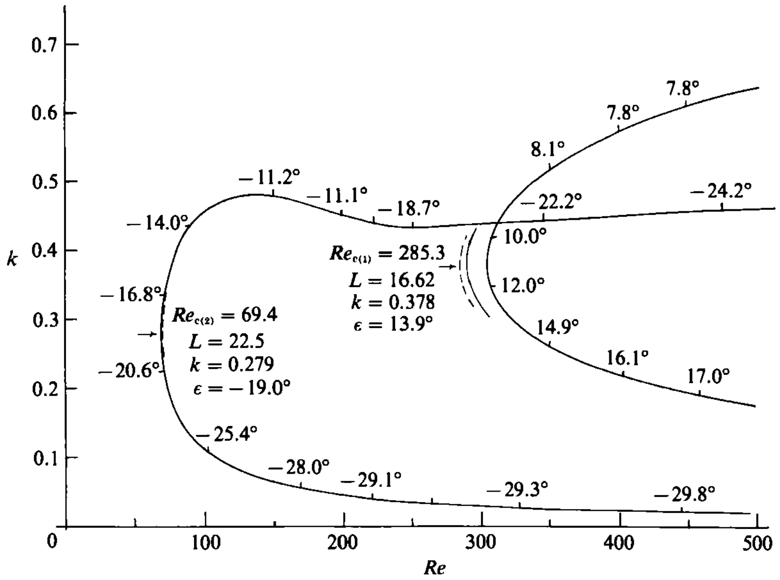

FIGURE 6. Three-dimensional neutral curves for the von Kármán layer and for the Type 1 and Type 2 instabilities. Values of ϵ are given at selected points on the curves. The thicker solid lines are for $\Delta z = 0.4$, the thinner line is for $\Delta z = 0.2$, and the dashed line is an extrapolation to $\Delta z = 0$.

instability might be expected to first reach finite amplitude when random disturbances excite Type 2 (§5).

The lines of constant C_p in figure 5 show that both Type 1 and Type 2 can have $C_p = 0$, and the low-k lobe on the neutral curve found by Malik (1986) for stationary disturbances at $Re = 441$ probably was the Type 2 instability.

The neutral curves of figure 2 do not sharply select the values of Re_c, but this has been done with a three-dimensional neutral-curve follower that produced the curves of figure 6. $\Delta z = 0.4$ was used for the full curves, but near Re_c, Δz was reduced to 0.2 (thin 'bow shock' line) and an extrapolation was made to $\Delta z = 0$ (dashed lines). For Type 1 the correction was substantial but for Type 2 it was less than the inaccuracy of the drawn graph. The angles ϵ are given at selected points along the curves.

Figure 7 shows patterns of ϕ and u for one example of Type 1 and two examples of Type 2 that are of interest later for their energy cycles (§4.3). Figures 7 (*a*) and 7 (*b*) correspond closely to the conditions of maximum α in figure 4. Figure 7(*c*) is an example with large C_p as reflected in the tilt of the pattern. The zero lines of $\phi(z)$ and $u(z)$ may be thought of as eigenfunctions.

4.2. *The Ekman and Bödewadt layers*

Figure 8 shows three-dimensional neutral curves for the Ekman layer ($Ro = 0$) and the Bödewadt layer ($Ro = 1$). As with the von Kármán layer, the Type 1 and Type 2 curves are clearly separated by angle. But whereas in the von Kármán layer both branches of both curves could be followed to above $Re = 500$, such was not the case for these two boundary layers. In following the Type 2 (lower) curve for the Ekman layer toward increasing k, when a point near $k = 0.44$ was reached the angle of maximum instability shifted rapidly from $\epsilon = -18°$ to $\epsilon = 5°$, from Type 2 to Type 1. Similarly, when the Type 1 (upper) curve was followed downward the shift to Type 2 occurred at about $k = 0.384$, a shift from 4° to −20°. For the Bödewadt layer the

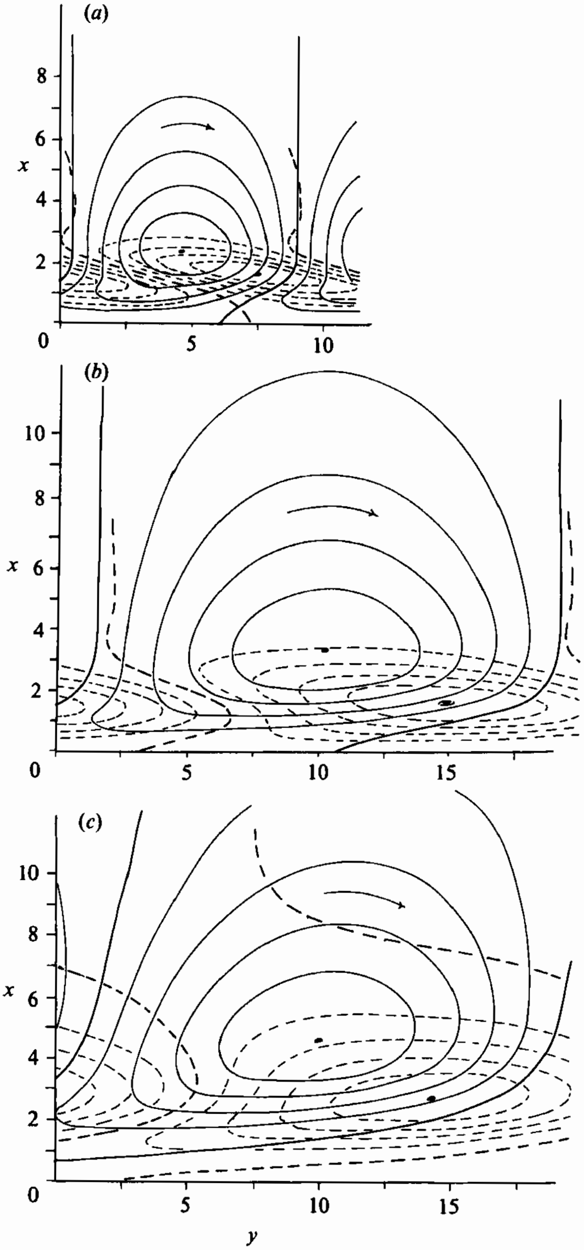

FIGURE 7. Patterns of stream function ϕ (solid lines) and the x-component of flow, u, (dashed lines) in the (y, z)-plane. (a) Type 1 for $Re = 400$, $L = 17$, and $\epsilon = 15$. (b) Type 2 for $Re = 400$, $L = 35$ and $\epsilon = -5°$. (c) Type 2 for $Re = 400$, $L = 35$ and $\epsilon = -30°$.

Type 1 curve never reached a clear maximum before the computation automatically shifted to Type 2. These shifts reflect certain features of the three-dimensional neutral surfaces.

For the Ekman layer ($Ro = 0$) the differential equations are exact and the computational results are accurate. For the Bödewadt layer, however, the critical value of Re is very low ($Re_{c(2)} = 15.1$) and the errors due to the various approximations made in §2 should be more serious than for the von Kármán layer.

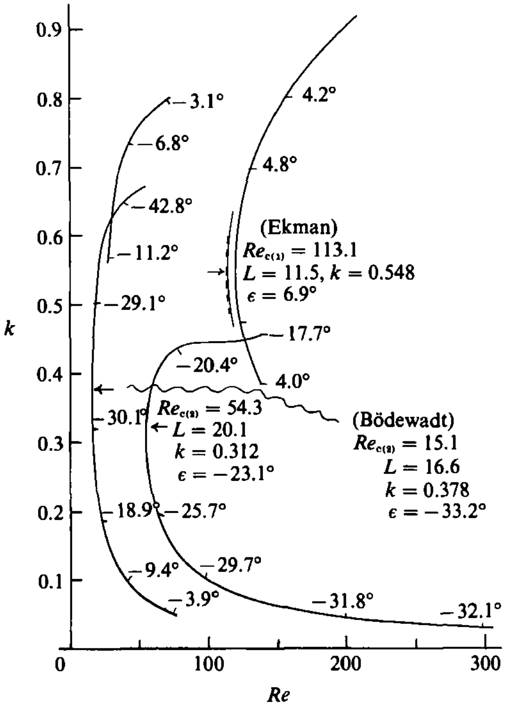

FIGURE 8. Neutral curves similar to those of figure 6 but for the Ekman and Bödewadt layers.

Although the Bödewadt layer results are here limited to neutral curves, it is notable that above only $Re = 25$ Type 1 has larger growth rates than Type 2. Since good experiments below $Re = 50$ are almost impossible to attain, the instability seen in Bödewadt layer experiments is usually Type 1.

4.3. *Energy budgets*

Kinetic energy equations have been derived from (21) and (22) with $Ro = -1$ by multiplying by u and by $-\phi$, respectively, and averaging over y and z (overbars) to obtain

$$\frac{\partial CK}{\partial t} = \underbrace{-Re\,\overline{V_z vw}}_{\mathrm{I}} \underbrace{-(\overline{H\xi v}+\overline{Fv^2})}_{+\ \mathrm{IV}} \underbrace{-2(1-G)\,\overline{uv}}_{+\ \mathrm{III}} \underbrace{-(\overline{v_y^2}+\overline{v_z^2}+\overline{w_y^2}+\overline{w_z^2})}_{+\ \mathrm{VI}}, \tag{24}$$

$$\frac{\partial UK}{\partial t} = \underbrace{-Re\,\overline{U_z uw}}_{\mathrm{II}} + \underbrace{(\overline{H(u^2/2)_z}+\overline{Fu^2})}_{\mathrm{V}} + \underbrace{2(1-G)\,\overline{uv}}_{-\ \mathrm{III}} \underbrace{-(\overline{u_y^2}+\overline{u_z^2})}_{+\ \mathrm{VII}}. \tag{25}$$

Terms I and II represent the extraction of energy from the basic flow by the Reynolds stresses. Term III is the Coriolis/centrifugal exchange from *UK* to *CK*. Terms IV and V are *Ro* terms and thus depend upon the geometrical effects of the change of *Re* with radius. As defined, the *Ro* terms turn out to be always negative and therefore extract energy from both *CK* and *UK*. Curiously the *Ro* terms for *CK* involve only v and w while the *Ro* terms for *UK* involve only u. The energy budget is completed by the negative definite viscous dissipation terms VI and VII.

Figure 9 illustrates the energy budgets for the three combinations of *Re* and k used for figure 7. Figure 9(*a*) is for Type 1. There Term I is the only source of energy for *CK*, and the Coriolis/centrifugal transfer is from *CK* to *UK*. Term II, the generation

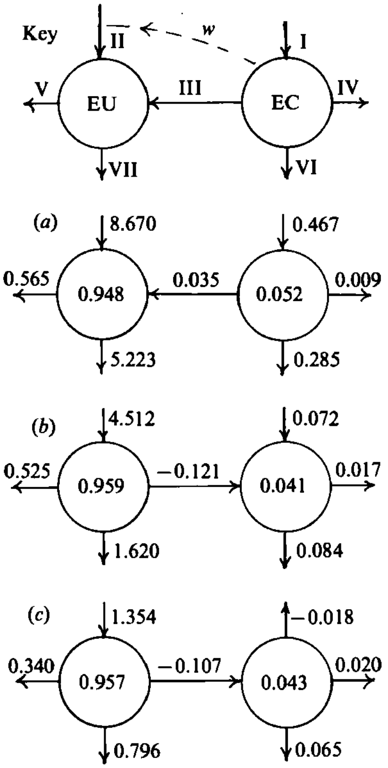

FIGURE 9. Energy flow diagrams. The 'key' refers to equations (24) and (25); (*a–c*) correspond to (*a–c*) of figure 7.

of *UK* by the basic flow, is by far the dominant term, and *UK* turns out to contain much more energy than *CK*. But the dashed arrow in the key indicates that w, from the cells, is essential for Term II, and so the existence of cells is essential to the generation of *UK* by the basic flow.

Figure 9(*b*) is for Type 2 (also figure 7*b*) where the cells are now driven more by Term III than by Term I. This is characteristic of the Type 2 instability.

Figure 9(*c*) is an example where Term I transfers energy *to* the basic flow *from* the cells, an example of negative eddy viscosity. Here the only source of energy is to *UK* by Term II. The cells (*CK*) are then supported entirely by a transfer from *UK* by Term III. This cycle is clearly a 'bootstrap' operation. The cells are essential, through w, for the primary energy transfer to the fluctuations, u, by Term II, and u in turn is necessary for the Coriolis/centrifugal maintenance of the cells, Term III. These different energy transfer cycles must be reflected in the patterns of ϕ and u in figure 7, but it is not easy to visually detect the essential differences.

4.4. *Group velocities*

A major goal is to determine the radial propagation and growth of Type 2 instabilities to assess their importance for transition. For this purpose the group velocity $C_g(Re, \epsilon, L)$ has been calculated from the array of $C_p(Re, \epsilon, L)$.

Spooner & Criminale (1982) have shown, for small-amplitude unstable disturbances in the Ekman layer, that group velocities can be quite accurately determined from the standard kinematic formula. Similar computations by this author and Mr Shen-Teng Yang (unpublished) have confirmed those results.

		Wavelength, L		
Re		20	25	30
480	C_{gr}	0.0757	0.0687	0.0580
	C_{gt}	0.4974	0.5030	0.5160
400	C_{gr}	0.0751	0.0640	–
	C_{gt}	0.5074	0.5120	–

TABLE 4. Group velocity components for the Type 1 instability at $\epsilon = 15$ as a function of L and *Re*. Top, the radially outward component, C_{gr}. Bottom, the tangential component, C_{gt}, relative to the disk and opposite to the direction of rotation.

		Wavelength, L							
Re		20	25	30	35	40	45	50	55
480	C_{gr}	—	0.1191	0.1206	0.1232	0.1258	0.1287	0.1317	0.1351
	C_{gt}	—	0.7572	0.7479	0.7371	0.7248	0.7143	0.7030	0.6923
400	C_{gr}	—	0.1201	0.1215	0.1244	0.1281	0.1312	0.1338	0.1370
	C_{gt}	—	0.7514	0.7397	0.7262	0.7133	0.7009	0.6890	0.6791
320	C_{gr}	—	0.1213	0.1235	0.1266	0.1297	0.1335	0.1378	0.1411
	C_{gt}	—	0.7406	0.7260	0.7104	0.6968	0.6849	0.6731	0.6648
240	C_{gr}	0.1205	0.1230	0.1264	0.1306	0.1340	0.1384	0.1419	0.1454
	C_{gt}	0.7443	0.7227	0.7056	0.6903	0.6785	0.6677	0.6599	0.6533
160	C_{gr}	0.1231	0.1269	0.1314	0.1357	0.1399	0.1444	0.1488	0.1526
	C_{gt}	0.7169	0.6974	0.6832	0.6727	0.6643	0.6572	0.6526	0.6483
80	C_{gr}	0.1291	0.1337	0.1387	0.1445	0.1495	0.1543	0.1602	—
	C_{gt}	0.6929	0.6838	0.6780	0.6744	0.6710	0.6696	0.6688	—

TABLE 5. The same as table 4 but for the Type 2 at $\epsilon = -15$.

The group velocity can be found from

$$C_g = -\nabla_k \sigma \tag{26}$$

where σ is the wave frequency and the operator ∇_k refers to the gradient with respect to the components of k in wavenumber space. Thus in rectangular coordinates using k_x and k_y as the wavenumber components

$$C_g = \boldsymbol{i}\,\partial\sigma/\partial k_x + \boldsymbol{j}\,\partial\sigma/\partial k_y, \tag{27}$$

and in polar coordinates, here using the variates k and ϵ,

$$C_g = \boldsymbol{n}\,\partial\sigma/\partial k + \boldsymbol{p}\,\partial\sigma/k\,\partial\epsilon, \tag{28}$$

where the unit vectors $\boldsymbol{p}$ and $\boldsymbol{n}$ are parallel and normal to the waves, respectively. The polar form also can be written as

$$C_g = \boldsymbol{n}(C_p - L\,\partial C_p/\partial L) + \boldsymbol{p}\,\partial C_p/\partial\epsilon \tag{29}$$

which is particularly suitable for this study where values of C_p have been determined over an array of values of L and ϵ. In Appendix B (29) is derived directly by what is thought to be a novel approach.

Tables 4 and 5 give examples of the radial and tangential group velocity components, C_{gr} and C_{gt}. From table 4 the group speed averages about $C_g = 0.51$, and the angle of C_g relative to the tangent ranges from 6.4° to 8.5°. Curiously it is possible for the group velocity to be exactly along the direction of the vortices for angles in the vicinity of $\epsilon = 8°$, and in such a case 'Venetian blind effect' (Appendix B) would seem to be an appropriate descriptive term.

This nearly tangential direction of the group velocity was found by Cebeci & Stewartson (1980) who analysed the relevant Orr–Sommerfeld equation and noted that 'disturbances begin by travelling outward but at a very small, almost constant, angle ($\sim 8°$) to the negative of the direction of the motion of the disk, i.e. they are left behind by the rotating disk'. In table 4 all values of C_{gr} are positive whereas the phase speeds at $\epsilon = 15°$ (table 1) all have an inward (negative) component.

Figures 3 and 11 from Wilkinson & Malik (1985) show normalized wave forms as a function of radius and azimuth angle from hot-wire measurements of a velocity component, u', for a stationary Type 1 instability. From those patterns one can clearly see and measure the direction of energy propagation. The angles of four conspicuous patterns are $8.4 \pm 1.4°$, $8.5 \pm 2.5°$, $9.5 \pm 2.8°$ and $9.5 \pm 3.7°$, where the limits indicate estimates of the apparent widths of each wave group. The average angle is then 9.0° with an average spreading angle of 2.6°. Thus the experimental and numerical results on the direction of $\boldsymbol{C}_g$ are in excellent agreement.

Over the range of table 5 the angles of propagation vary from 8.9° to 13.4° to the tangent, and the speeds, relative to the disk, vary from 0.766 to 0.682. Experiments by the author using dye in a rotating tank of water have shown angles of propagation in good agreement with the computational results. Thus, as in the Ekman layer (Spooner & Criminale 1982) the $\boldsymbol{C}_g$ are not much different for Type 1 and Type 2. In retrospect one should not be surprised by this result because these are advected instabilities that both extend well into the basic flow (figure 7), not waves following independent wave equations. From tables 4 and 5, C_g for Type 1 is consistently less than for Type 2, perhaps because Type 1 cells do not extend as far out of the boundary layer.

5. The radial propagation and growth of disturbances

The rate of growth of amplitude with radius for a disturbance may be written as

$$\mathrm{d} \ln A/\mathrm{d}r = \alpha/(-2Re\, C_{gr}), \tag{30}$$

where Re appears in the denominator because of the method of non-dimensionalization, and the factor $\frac{1}{2}$ arises because $\mathrm{d} \ln A/\mathrm{d}t = \frac{1}{2}\alpha$. Upon integration, noting that in non-dimensional form $r = -Re$,

$$\ln\left(\frac{A}{A_0}\right) = \int_{Re_0}^{Re} \frac{\alpha}{2Re'\, C_{gr}} \mathrm{d}Re', \tag{31}$$

where α and C_{gr} are functions of Re. Ln (A/A_0) is sometimes called the N-factor, and according to Bushnell, Malik & Harvey (1988) N-factors of 9–11 are associated with transition to turbulence in a wide range of undisturbed three-dimensional boundary layers. Indeed, Wilkinson & Malik (1985) found N-factors of about $N = 10$ from hot-wire measurements of the stationary mode on a rotating disk. But at what values of L and ϵ should $\alpha(Re)$ and $C_{gr}(Re)$ be evaluated if (31) is to be integrated to find the radial growth of disturbances?

In the circular geometry equiangular spiral waves cannot maintain constant spacing with radius, and the tendency of the waves to be at some fixed angle is in conflict, in a sense, with the tendency for a fixed spacing. There must be some accommodation of angle and wavelength as the energy of a disturbance propagates

Mode (ϵ, L)	Re_c	*Re* 200	280	360	440	520
(10, 20)	310	—	—	0.61	3.33	7.43
(15, 20)	300	—	—	1.19	4.60	9.63
(−20, 25)	69	1.43	2.32	3.14	3.42	4.66
(−15, 30)	78	1.75	3.21	4.50	5.62	6.62
(−10, 30)	87	0.93	2.61	4.25	5.88	7.14
(−5, 30)	102	1.12	2.71	4.39	6.01	7.50
Variable	69	1.90	3.56	5.22	6.91	8.57

TABLE 6. $N = \ln(A/A_0)$ as a function of *Re* for several different modes of instability. First 2 rows: Type 1 modes. Rows 3–6: Type 2 modes. The last row is based upon the maxima of $\alpha/2Re\,C_{gr}$ as a function of *Re*.

radially. This problem arises from the representation of the disturbances by Fourier modes in a rectangular coordinate system. Presumably only a complete three-dimensional solution of the stability problem can represent the radial development of disturbances without ambiguity, and in the present study there can be no strict basis upon which to choose the values of ϵ and L, and therefore α and C_{gr}, as r changes.

In spite of these shortcomings estimates of the growth of disturbances have been made by determining $\alpha(Re)$ and $C_{gr}(Re)$ in two different ways. In table 6 the radial growths of selected modes with fixed values of ϵ and L are presented. Of the two examples of Type 1, mode (15, 20) attains $N = 9.63$ at $Re = 520$, a growth nearly identical to the observed points of figure 8 in Wilkinson & Malik (1985). Of the four examples of Type 2, mode $(-5, 30)$ starts at the largest $Re_{c(2)}$ but soon attains larger values of N than the other modes, reaching $N = 7.5$ at $Re = 520$.

In the second method the maxima of $(\alpha/2Re\,C_{gr})$ (allowing ϵ and L to change with *Re*) have been used in (31). This method gave $N = 8.47$ at $Re = 520$. Thus the correct value for Type 2 instabilities probably lies in the interval $7.5 < N < 8.5$ if the Fourier representation gives reasonable estimates of the local values of α and C_{gr}. The two methods do not differ greatly because C_{gr} does not vary much with *Re*, ϵ, and L, and because the second method is dominated by values of α close to those of mode $(-5, 30)$.

As with Type 2, the precise Type 1 mode that one should expect in an experiment is not certain. Table 7 gives values of C_p, C_{gr} and α at $Re = 400$ and at $Re = 520$. There it can be seen by interpolation that: (i) the most unstable mode varies slightly with *Re*; (ii) the stationary mode, $C_p = 0$, is not quite the same as the most unstable mode (also see figure 5); and (iii) for all Type 1 modes $C_{gr} > 0$ even though C_p may be negative (table 1).

If fixed disturbances on a disk trigger instability, as in experiments discussed by Wilkinson & Malik (1985), one should expect Type 1 to be stationary. Stationary vortices need not always occur, however, and in rotating disk experiments with water (and dye) over a clean glass plate Type 1 often has been seen to move. Although data are not available for the von Kármán layer, non-zero values of C_p have been observed for Type 1 waves in the Ekman layer at angles from 6.1° to 15.1°, as documented in Faller (1963).

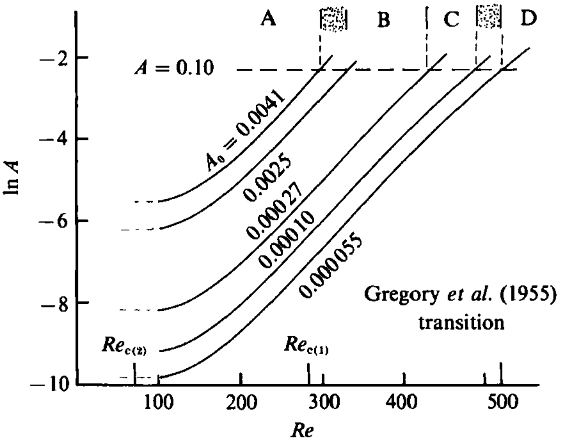

FIGURE 10. Four transition mechanisms, A, B, C, and D, dependent upon the initial amplitude excitation, A_0, of Type 2 vortices by the free-steam flow. The curves, based upon disturbances with $\epsilon = -5$ and $L = 30$, illustrate the growth of amplitude, A, as a function of Re, starting from different A_0.

	$Re = 400$			$Re = 520$		
L	10	15	20	10	15	20
			C_p			
15	0.0132	−0.0325	−0.0749	0.0137	−0.0308	−0.0720
20	0.0206	−0.0255	−0.0683	0.0205	−0.0243	−0.0659
25	0.0308	−0.0159	−0.0584	0.0294	−0.0157	−0.0576
			C_{gr}			
15	0.0807	0.0751	—	0.0945	0.0756	—
20	0.0701	0.0640	—	0.0823	0.0694	—
25	—	—	—	—	—	—
			α			
15	2.444	2.613	2.153	5.078	5.047	4.870
20	2.199	2.614	2.522	4.995	5.597	5.520
25	0.986	1.502	1.547	3.760	4.381	4.439

TABLE 7. Values of C_p, C_{gr} and α for selected modes of the Type 1 instability at $Re = 400$ and at $Re = 520$.

6. Transition mechanisms

Gregory *et al.* (1955) found transition from undisturbed flow at the average Reynolds number of $Re_t = 523 \pm 13$ (one standard deviation from 9 measurements) while Wilkinson & Malik (1985) found transition for a clean plate in the range $543 < Re_t < 556$. Because the precise point of transition is a matter of definition and may depend upon the observational method, and because growth rates in the present study were obtained routinely only to $Re = 520$, the nominal value is taken here to be $Re_t = 520$.

The linearized numerical results can only bring instabilities to some reasonable amplitude, say $A = 0.1$, before nonlinear interactions become important, and they can say nothing directly about transition mechanisms. But the linearized growths allow us to speculate on different transition mechanisms that may occur according to the relative amplitudes of the Type 1 and Type 2 vortices together with the speed of the basic flow, as represented by Re.

Figure 10 supposes four possible transition mechanisms. The ranges of A_0 and Re for these can only be approximated, and the curves of $\ln(A)$ *vs.* Re are based upon only the single mode $(-5, 30)$ for illustration. The scheme of figure 10 is based in part upon three-dimensional computations for the Ekman layer by Ugo Piomelli and this author, reported in part in Faller *et al.* (1989), where it has been found that at certain values of Re finite-amplitude Type 2 vortices can suppress the growth of linearly unstable Type 1 modes, and, conversely, existing finite-amplitude Type 1 vortices can suppress the growth of linearly unstable Type 2 modes.

Mechanism A occurs when the external random disturbances give rise to initial amplitudes $A_0 > 0.0051$, approximately. (The corresponding Re value when $A = 0.1$ is 300.) For $A_0 > 0.0051$ several Type 2 modes will grow and reach finite amplitude more or less simultaneously and will interact to produce a spectrum of low-level turbulence, and as Re increases the turbulence will gradually develop.

If the external disturbances give $A_0 < 0.0051$, the single Type 2 mode that grows most rapidly will become of large amplitude and will suppress other modes as it interacts nonlinearly with the basic flow. This interaction will not produce a secondary instability (Mechanism B) if Re is too small. Thus there can be a range of A_0 (stippled region of figure 10) in which a single finite-amplitude Type 2 mode, plus its harmonics, dominates without transition. The experiment of figure 11 below $Re = 356$ appears to be such an example.

Transition will occur when some combination of the dominant Type 2 mode and Re are large enough (Mechanism B). A secondary instability (ribs) of much smaller scale and nearly perpendicular to the primary Type 2 vortices arises and rapidly interacts with the primary vortices to produce turbulence. This occurred in the experiments of Faller & Kaylor (1966*a*), and a more detailed description is given in §7.

Type 1 is first unstable at $Re_{c(1)} = 285$ and it seems likely that there will be some range of Re where, with a certain low level of excitation of Type 2, both Type 1 and Type 2 will reach finite amplitude in the same range of Re. In the scheme of figure 10 this range is $430 < Re < 490$ and the corresponding initial amplitude range for Type 2 is $0.0027 > A_0 > 0.0010$. Then the two waves may be expected to interact nonlinearly (Mechanism C) to generate other modes and to produce a full spectrum of turbulence. Although examples of this mechanism are not documented, ciné film sequences indicate the reality of Mechanism C in certain cases.

For $0.00010 > A_0 > 0.000055$ it is supposed that Type 1 will attain a sufficiently large amplitude to suppress the growth of Type 2 but will still be too small to produce transition by interaction with the basic flow. Thus there may be a second range, $490 < Re < 520$ (stippled, corresponding to the indicated range of A_0) where transition does not occur if only this single Type 2 mode is excited.

Above $Re = 520$ the interaction of Type 1 with the basic flow (Mechanism D), is believed to lead to transition. Wilkinson & Malik (1985) have shown the presence of higher wavenumber fluctuations as transition is approached, so the detailed mechanism may again involve the generation of a secondary instability.

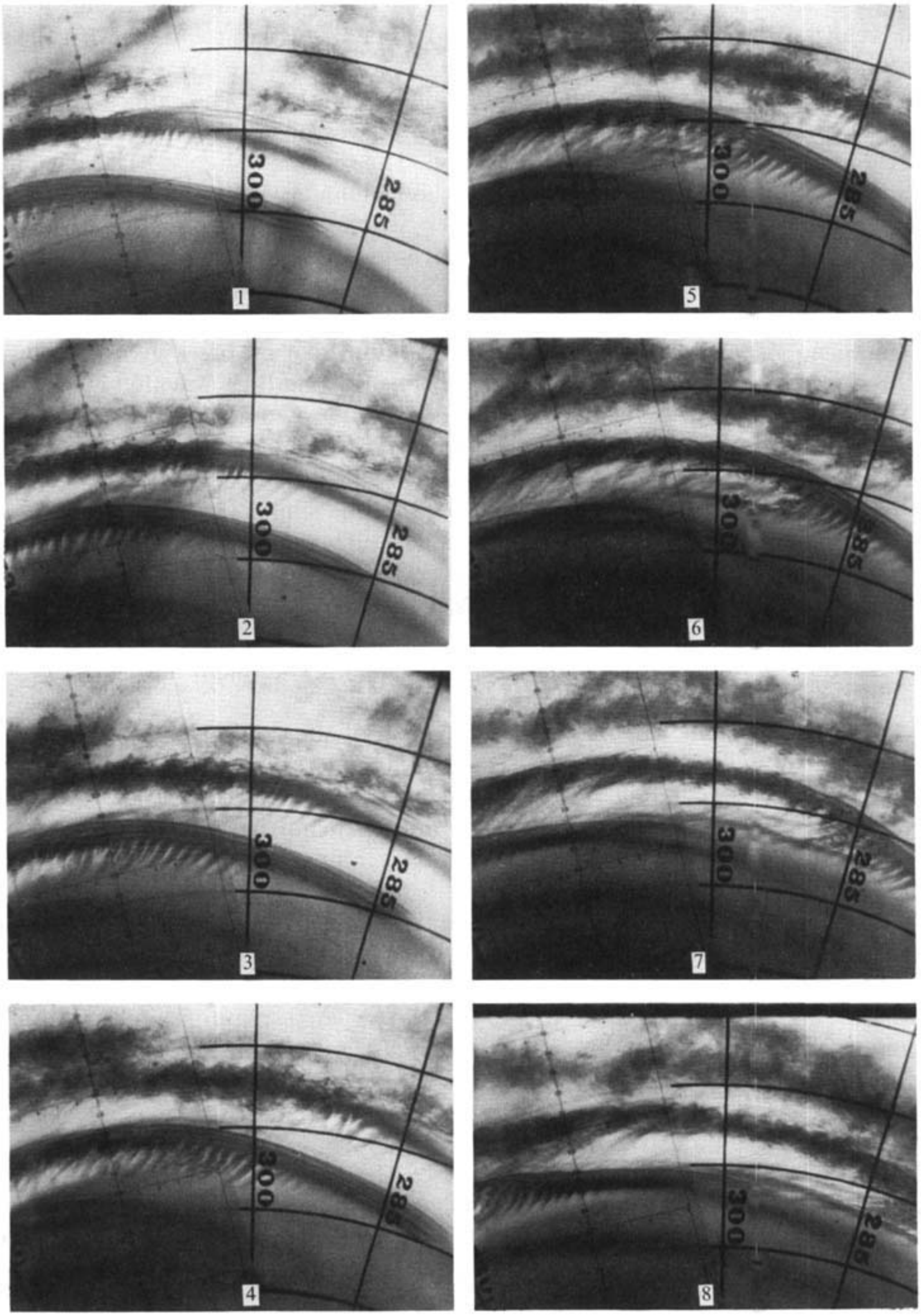

FIGURE 11. Photographs at intervals of 0.342 s that illustrate transition by Mechanism B. The tank radius is 114 cm, $H = 15$ cm, $\Omega = 0.325\ \mathrm{s}^{-1}$, $\nu = 0.99\ \mathrm{cm}^2\ \mathrm{s}^{-1}$, and the water was initially at rest. The circular lines of the background grid are at $r = 50, 60, 70$, and 80 cm ($Re = 285, 343, 400$, and 467), and the radial lines are at intervals of 15°. This grid, and an auxiliary rectangular grid (left), are beneath the smooth plate-glass boundary. The dye is methylene blue and is moving outward in the boundary layer after being poured in at the centre of the tank to inject the dye and to create disturbances.

7. A transition experiment

The sequence of figure 11 shows the appearance of the secondary instability (ribs) in a series of three bands of dye as they move outward and undergo transition by Mechanism B. In this series the ribs are first visible at about $r = 68$, 62, and 67 cm ($Re = 390$, 356, and 385), and turbulence appears at about $r = 70$ cm ($Re_t = 402$). As with the primary instability the dark dye bands of the ribs are interpreted as regions where there has been upward motion to produce a thicker layer of dye while the clear spaces between the ribs are regions where there has been downward motion. Note that the ribs sometimes develop a two-band structure (a clear space in the middle of each rib) suggesting the existence of a strong first harmonic of the rib wavelength.

The nature of the secondary instability has not been clearly identified. Although in figure 11 the ribs are nearly perpendicular to the Type 2 bands, on other occasions they have been observed at an angle closer to that expected of Type 1. A proper theory of the secondary instability must consider the complex three-dimensional flow that is the sum of the basic flow and the Type 2 vortices.

Average characteristics of the primary bands and of the ribs are given in table 8 but these values are for only the one sequence of events in figure 11. Dye bands from the same ciné film at an earlier time showed very small negative angles, different spacings, etc. Even within the analysed sequence there are substantial variations in spacing and other characteristics, and the analysis is somewhat subjective. These variations probably are caused by a lack of uniformity in the stimulation of the instability near the centre of the tank, which came from simply pouring in the dyed water, but variation may also arise from the adjustments of spacing and angle that must occur as the vortices move outward. Note from table 8 that the observed band spacing $L = 53.9$ is substantially larger than that of the most unstable wavelength from the numerical model. This might be due to the equiangular spreading of bands that formed with a lesser spacing at a lower radius.

The closeness of the observed and numerical values of C_p, 0.353 and 0.357, respectively (table 8) is better than should be expected from the accuracy of the observations. Also in good agreement are the tangential speed of the ribs and the computed tangential group velocity. Note that these values are both only about one half the apparent tangential speed at which a band intersection moves along a circular arc, in this case $C_p/\sin\epsilon = 1.29$.

8. Conclusions

The characteristics of the instabilities of the von Kármán (rotating disk) boundary layer have been numerically computed for a large range of the parameters Re, ϵ, and L. The results include growth rates, phase speeds, group velocities, the ratio of the energy of the longitudinal fluctuations to that of the overturning cells, and the cell structures. Wherever comparisons can be made the results are generally in excellent agreement with previous computational results and with available experimental data. The complete tabulated data and extended discussions of the results are available in technical notes (Faller *et al.* 1989; Faller 1990).

The nature of the secondary instability has not been clearly identified. A proper theory must consider the complex three-dimensional flow that is the sum of the basic flow and the finite-amplitude Type 2 vortices. A factor of possible importance is the ratio RK. From table 3 we find ratios in the range $15 < RK < 50$, suggesting ratios of u to v or w between 5 and 8. For Ekman-layer instability RK is the order of 2, and

Average radius of measurements	61.4 cm ($Re = 352$)
Average angle	$-15.4°$
Average wavelength	9.4 cm ($L = 53.9$)
Computational wavelength for maximum α at $Re = 350$, and $\epsilon = -15$	$L = 38$
Average normal speed (phase speed)	6.84 cm s^{-1}
Observed phase speed	0.343
Computational phase speed, C_p	0.347
Wavelength of ribs	
Parallel to bands	1.64 cm
Non-dimensional	9.4
Tangential speed of individual ribs	0.666
Computational group velocity, C_{gt}	0.671

TABLE 8. Average characteristics of the primary dye bands (Type 2 instability) and ribs (secondary instability) in the sequence of figure 11.

in the Bödewadt layer *RK* is typically less than 1. Similar secondary instabilities have not been found in the Ekman and Bödewadt layers, and the relatively large values of u in the von Kármán layer suggest that the longitudinal fluctuations, u, may play a significant role in the mechanism of the secondary instability.

The Type 2 instability is the probable source of early transition when the external flow is subject to random turbulent fluctuations. With such fluctuations the Reynolds number of transition and the mechanism of transition should depend upon the level of excitation of the Type 2 instability. Several proposed mechanisms, supported in part by laboratory experiments and in part by three-dimensional modelling of the unstable Ekman layer, are proposed. These are, in order of decreasing amplitude of the disturbances: A, the interaction of several Type 2 modes; B, the interaction of a dominant Type 2 mode with the basic flow to produce a secondary instability; C, the interaction of Type 2 and Type 1 modes; and D, the interaction of a dominant Type 1 mode with the basic flow to produce a secondary instability.

The author is grateful to the National Science Foundation for support under Grant MSM 8617897. Special thanks are extended to Professor Ugo Piomelli with whom extensive computations on transition mechanisms in the three-dimensional Ekman layer have been carried out using the Cray X/MP at the San Diego Supercomputer Center.

Appendix A. Timescales and growth rates

In this study, and in Faller & Kaylor (1966*b*) for the Ekman layer, it has been found that near $Re_{c(1)}$ the growth rate of the Type 1 instability is nearly linear with $Re - Re_{c(1)}$, and near $Re_{c(2)}$ the growth rate of Type 2 increases more or less as $(Re - Re_{c(2)})^{\frac{1}{2}}$. Some may find these results to be at odds with those of Lilly (1966), Spooner & Criminale (1982), and others, but the difference lies simply in the non-dimensionalization of time.

In Lilly (1966) non-dimensional time is defined by

$$t(L) = tU/D, \tag{A 1}$$

where U is a basic-flow scaling velocity and D is the boundary-layer depth, a scaling common to many boundary-layer studies particularly in non-rotating systems where there is no natural timescale. Here and in Faller & Kaylor (1966*b*) time has been scaled as

$$t(F) = t\Omega, \tag{A 2}$$

where Ω^{-1} is the natural timescale of the system due to rotation.

Equating t from (A 1) and (A 2) one finds

$$t(L) = Re\, t(F), \tag{A 3}$$

and it follows that the corresponding growth rates are related by

$$\alpha(L) = Re^{-1}\alpha(F). \tag{A 4}$$

Then if the growth rate for Type 1 is given by

$$\alpha(1,F) = a(Re - Re_{\mathrm{c}(1)}), \tag{A 5}$$

it follows that

$$\alpha(1,L) = a(1 - Re_{\mathrm{c}(1)}/Re). \tag{A 6}$$

Similarly, if we assume that for Type 2

$$\alpha(2,F) = (a + b(Re - Re_{\mathrm{c}(2)})^{\frac{1}{2}} \tag{A 7}$$

then

$$\alpha(2,L) = ((a/Re)^2 + b(Re^{-1} - Re_{\mathrm{c}(2)}/Re^2))^{\frac{1}{2}} - a/Re. \tag{A 8}$$

Thus, for this simple representation $\alpha(2,L) \rightarrow 0$ as $Re \rightarrow \infty$, but this is not true of $\alpha(2,F)$.

Appendix B. A polar coordinate interpretation of group velocity

From (29) one can write

$$\boldsymbol{C}_{\mathrm{g}} = \boldsymbol{n}(C_{\mathrm{p}} - C_{\mathrm{gd}}) + \boldsymbol{p}C_{\mathrm{g}\theta} \tag{B 1}$$

where $C_{\mathrm{gd}} = -L\,\partial C_{\mathrm{p}}/\partial L$ may be called the 'normal deficit', it being a deficit from the phase speed, and $C_{\mathrm{g}\theta} = \partial C_{\mathrm{p}}/\partial\theta$ may be called the 'parallel component', it being a component of $\boldsymbol{C}_{\mathrm{g}}$ parallel to the wave crests. Thus for waves in which both C_{gd} and $C_{\mathrm{g}\theta} = 0$, $\boldsymbol{C}_{\mathrm{g}} = \boldsymbol{C}_{\mathrm{p}}$.

To derive $C_{\mathrm{g}\theta}$ consider two waves with the same L but with $C_{\mathrm{p2}} > C_{\mathrm{p1}}$, and with Wave 2 at a small angle $\Delta\theta$ to Wave 1 as in figure 12. Subtract out the velocity C_{p1} so that Wave 1 appears to be fixed. Then the time required for the initial interference pattern to first be repeated by the motion of Wave 2 relative to Wave 1 is simply

$$T = L/(C_{\mathrm{p2}} - C_{\mathrm{p1}}\cos\Delta\theta). \tag{B 2}$$

The interference pattern can be characterized by the intersections of the wave maxima, and during time T an intersection moves from A to B, a distance

$$Y = L/\sin\Delta\theta. \tag{B 3}$$

The apparent speed of propagation of energy to the left is simply

$$C_{\mathrm{g}y} = Y/T = (C_{\mathrm{p2}} - C_{\mathrm{p1}}\cos\Delta\theta)/\sin\Delta\theta, \tag{B 4}$$

and as $\Delta\theta \rightarrow 0$, $C_{\mathrm{g}y}$ becomes

$$C_{\mathrm{g}y} = \Delta C_{\mathrm{p}}/\Delta\theta. \tag{B 5}$$

If ΔC_{p} were held fixed while $\Delta\theta$ was reduced, the pattern would move ever more rapidly to the left. This phenomenon is commonly observed when viewing some nearly horizontal lines (e.g. telephone wires) through venetian blinds, and the

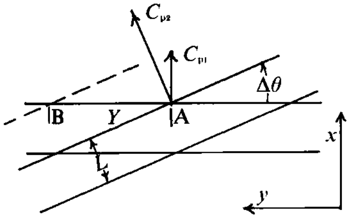

FIGURE 12. Group propagation by the relative motions of superimposed wave trains with the same wavelength, L, but with differing phase speeds. C_{p1} and C_{p2}, and at an angular difference $\Delta\theta$.

illusion is appropriately called the 'venetian blind effect'. In a physical wave problem, however, ΔC_p will be a function of $\Delta\theta$, in general, and the appropriate limiting expression for the rate of propagation of the pattern, the apparent energy propagation rate, is, as $\Delta\theta \rightarrow 0$,

$$C_{g\theta} = \partial C_p/\partial\theta. \tag{B 6}$$

When this is a relatively large speed compared to the group velocity component along x, as is sometimes the case in rotating systems and as is the case in this study, the term 'venetian blind effect' may be appropriate for descriptive purposes.

C_{gd} is derived in a similar way. Consider two waves having small differences in wavelength, ΔL, and phase speed, ΔC_p, with $L_2 > L_1$ and $C_{p2} > C_{p1}$, but with $\Delta\theta = 0$. Starting where maxima of the two waves coincide, the time for the maximum of Wave 2 to overtake the next maximum of Wave 1 is

$$T = L_1/(C_{p2} - C_{p1}). \tag{B 7}$$

This is again the time for the interference pattern to first repeat itself when viewed relative to Wave 1. In this time the two wave maxima have travelled a distance

$$X = nL_1 = (n-1)L_2 \tag{B 8}$$

where n, the number of L_1 moved in time T, is given by

$$n = L_2/(L_2 - L_1). \tag{B 9}$$

By considering the interference pattern of the two wave trains during time T and relative to Wave 1, as in the derivation of $C_{g\theta}$, it is easily seen that: (i) the envelope of the interference pattern moves toward negative x; (ii) X is the wavelength of the envelope; and (iii) the pattern moves through $-X$ in time T. The relative speed of the group is thus given by

$$C_{gd} = -X/T = -L_2 \Delta C_p/\Delta L. \tag{B 10}$$

Taking C_p to be a function of L, as $\Delta L \rightarrow 0$ the equation for the group velocity deficit becomes

$$C_{gd} = -L\,\partial C_p/\partial L. \tag{B 11}$$

REFERENCES

BÜHLER, K. & ZIEREP, J. 1983 Transition to turbulence in a spherical gap. *4th Intl Symp. on Turbulent Shear Flows, Sept. 1983, Karlsruhe.*

BUSHNELL, D. M., MALIK, M. R. & HARVEY, W. D. 1988 Transition prediction in external flows via linear stability theory. *IUTAM Symp. Transonicum III, Göttingen.*

CEBECI, T. & STEWARTSON, K. 1980 On stability and transition in three-dimensional flows. *AIAA J.* **18**, 398–405.

Faller, A. J. 1963 An experimental study of the instability of the laminar Ekman boundary layer. *J. Fluid Mech.* **15**, 560–576.

Faller, A. J. 1990 Instability and transition of disturbed flow on a rotating disk. *Tech. Note* BN-1113. Inst. Phys. Sci. & Tech., University of Maryland.

Faller, A. J. & Kaylor, R. E. 1966*a* Investigations of stability and transition in rotating boundary layers. In *Dynamics of Fluid and Plasmas* (ed. S. I. Pai). Academic.

Faller, A. J. & Kaylor, R. E. 1966*b* A numerical study of the instability of the laminar Ekman boundary layer. *J. Atmos. Sci.* **23**, 466–480.

Faller, A. J., Yang, S. T. & Piomelli, U. 1989 Instability of the KEB boundary layers. *Tech. Note* BN-1102. Inst. Phys. Sci. & Tech., University of Maryland.

Gregory, N., Stuart, J. T. & Walker, W. S. 1955 On the stability of three-dimensional boundary layers with application to the flow due to a rotating disk. *Phil. Trans. R. Soc. Lond.* A **248**, 155–199 (referred to herein as GSW).

Iooss, G., Nielsen, H. G. B. & True, H. 1978 Bifurcation of the stationary Ekman layer flow into a stable periodic flow. *Arch. Rat. Mech. Anal.* **68**, 227–256.

Lilly, D. K. 1966 On the instability of Ekman boundary flow. *J. Atmos. Sci.* **23**, 481–494.

Mack, L. M. 1985 The wave pattern produced by point source on a rotating disk. *AIAA Aerospace Sciences Meeting, Jan. 14–17, Reno, Nevada, AIAA* 85-0490.

Malik, M. R. 1986 The neutral curve for stationary disturbances in rotating-disk flow. *J. Fluid Mech.* **164**, 275–287.

Malik, M. R., Wilkinson, S. P. & Orszag, S. A. 1981 Instability and transition in rotating disk flow. *AIAA J.* **19**, 1131–1138.

Smith, N. H. 1947 Exploratory investigation of boundary layer oscillations on a rotating disk. *NACA Tech. Note* 1227.

Spooner, G. F. & Criminale, W. O. 1982 The evolution of disturbances in the Ekman boundary layer. *J. Fluid Mech.* **115**, 327–346.

Wilkinson, S. P. & Malik, M. R. 1985 Stability experiments in the flow over a rotating disk. *AIAA J.* **23**, 588–595.